HAL open science

Modeling and control of conducting polymer actuator

Lingxiao Xun, Gang Zheng, Sofiane Ghenna, Alexandre Kruszewski, Eric Cattan, Christian Duriez, Sebastien Grondel

To cite this version:

Lingxiao Xun, Gang Zheng, Sofiane Ghenna, Alexandre Kruszewski, Eric Cattan, et al.. Modeling and control of conducting polymer actuator. IEEE/ASME Transactions on Mechatronics, 2023, 495-506, 10.1109/TMECH.2022.3211091 . hal-03852494

HAL Id: hal-03852494

https://hal.science/hal-03852494v1

Submitted on 29 Nov 2022

HAL is a multi-disciplinary open access archive for the deposit and dissemination of scientific research documents, whether they are published or not. The documents may come from teaching and research institutions in France or abroad, or from public or private research centers.

L'archive ouverte pluridisciplinaire **HAL**, est destinée au dépôt et à la diffusion de documents scientifiques de niveau recherche, publiés ou non, émanant des établissements d'enseignement et de recherche français ou étrangers, des laboratoires publics ou privés.

Modeling and Control of Conducting Polymer Actuator

Lingxiao Xun, Gang Zheng, *Senior Member, IEEE*, Sofiane Ghenna, Alexandre Kruszewski, Éric Cattan, Christian Duriez, Sébastien Grondel

***Abstract*—Conducting polymer actuator has nonlinear dynamic characteristics during its charge process. In this study, we proposed an electromechanic model and an optimal controller for a type of ionic electroactive polymer (IEPA) actuator with sub-millimeter scale, which can produce large deformation under low actuation voltage. The electronic model is to describe the evolution of charge state in time domain. The mechanic model is to calculate the deformation of conducting polymer actuator under the actuation force and external force. Based on the electromechanic coupling model, a parameter identification method is proposed to estimate the nonlinear parameter of conducting polymer actuator. The experiments show that our electromechanic model successfully predicts the deformation of actuator under different input voltages with the identified parameters. In the last step, an optimal controller is designed to control the orientation of IEAP actuator, which achieves at a high control performance in our experiments. The success of the modeling and control lays the foundation work for the subsequent biomedical applications.**

***Index Terms*—Conducting polymer actuator, IEAP, parameter identification, optimal control.**

I. Introduction

A. Review of relevant literature

Typical conducting polymer actuators are ionic polymer–metal composites and ionic electroactive polymer (IEAP). They have specific characteristics that allow them to be now used for various applications, whether in applications requiring actuation and/or sensing mode. The main advantage of these polymers based actuator is their soft nature, good stability, sufficiently high electric conductivity [1], bio-compatibility [2], large work density, low operating voltages (typically$\leqslant$3V) [3] that attracted a lot of attention over recent years for the realization of artificial muscles [4]. Moreover, their good electromagnetic compatibility, noise-free operation, low cost, light weight, their long life cycle [5] without degradation make these actuators a promising technology for microelectromechanical systems (MEMS). In addition, these polymers can be used as linear [6] or flexural micro-actuators [7], operating in solution [4] or in ambient air conditions [8]. Due to these advantages, they are implemented in a wide range of applications in robotics [9] or biomedical applications [3]. The work of this paper focuses on a typical actuator based on IEAP as the conducting polymer, which contains its nonlinear modeling, parameter estimation and control.

In this paper the IEAP based trilayer micro-actuator was micro-fabricated according to the method described in [7]. The upper and lower layers are made of electronically conducting polymers (CP) material basically poly(3,4-ethylenedioxythiophene) polystyrene sulfonate as reported in [10]. The middle layer is considered as an ion reservoir providing the system with ionic conductivity and mechanical properties [10]. This middle layer is formed with a semi-interpenetrated polymer network (IPN) composed of two polymers: poly ethylene oxide (PEO) and linear nitrile butadiene rubber (NBR) network. When a potential difference is applied to these two CP layers, one of the layers will undergo an oxidation reaction and the other one has a reduction reaction. It results in a corresponding increase or decrease in the charge density of the two layers. The change in ionic charge density will cause the two electrodes to produce opposite strains, which will cause one layer to expand and one layer to shrink. The expansion and contraction effect can be regarded as the bending of the actuator caused by the equivalent moment of force exerted on it. It should be noted that, the bending direction is occurring toward the anode [13].

Usually, an RC circuit model to describe the charge change process in the two electrode layers is used, and then the internal stress and strain are analyzed to obtain the curvature of the actuator. At present, some equivalent RC circuit models have been proposed [11], [12]. These models usually use isolated RC combinations or limited RC grid circuits to equivalent charge change processes. Although these models are efficient, their disadvantage is that they do not take into account the nonlinear changes of physical parameters in the actuator. The research of [14] shows that the resistivity and volumetric capacitance will both have greater nonlinearity during the charging process. The change interval affects the corresponding time of the actuator, so the nonlinear characteristics of the material are a consideration that can not be ignored in the modeling. [15] has proposed a finite nonlinear 2D-RC model, where this model takes into account the nonlinear characteristics of material properties following changes in charge density. In the work of Nishida [16], the infinite RC circuit was used to approximate the real system and finite difference method was adopted to get the numerical solution. However, the methods mentioned above struggle to achieve a balance between the dimensionality and accuracy of the model.

Lingxiao Xun, Gang Zheng, Alexandre Kruszewski, Christian Duriez are in Defrost team, Inria, university of Lille, Centrale Lille, CRIStAL - Centre de Recherche en Informatique Signal et Automatique de Lille - UMR 9189, France (e-mail: lingxiao.xun@inria.fr; gang.zheng@inria.fr; alexandre.kruszewski@centralelille.fr; christian.duriez@inria.fr).

Sofiane Ghenna, Éric Cattan and Sébastien Grondel are with Univ. Polytechnique Hauts-de-France, CNRS, Univ. Lille, Junia, Centrale Lille, UMR 8520 - IEMN, DOAE, F-59313 Valenciennes, France (e-mail: sofiane.Ghenna@uphf.fr; eric.Cattan@uphf.fr; sebastien.grondel@uphf.fr).

The second part of modeling for conducting polymer actuator is calculating its deformation. It is noticed that if the charging time is enough long to reach the equilibrium charge state, the deformation will be uniform along the polymer, leading to the uniform curvature, which has been calculated by several studies [11], [17]. In fact, it usually takes a long time to reach the equilibrium charge state, thus the local deformation is necessary to study. [16] and [18] proposed the Timoshenko model to predict the deformation of conducting polymer actuator with the assumption of small deformation of 2 degrees of freedom. Meanwhile, in most cases the conducting polymer actuator does not work alone but interacts with the environment, such as external forces applying on it or multi conducting polymer actuators being connected in series.

Another difficulty related to the nonlinear model lies in the measurement of electronic model parameters. The nonlinear changing of various physical parameters of materials requires a large amount of experimental data to construct. At the same time, it is difficult to realize the control of a single variable during the experiment due to the excessive change of material parameters, which affects the accuracy of the experimental results. This process is often cumbersome and is limited by measurement accuracy, resulting in error stacking.

In terms of drive control, [19] designed PID and adaptive robust controller for controlling the displacement of conducting polymer actuator. However, the above-mentioned controller design is only based on the system model after the end point displacement is identified, which does not include the actuator curvature and bending moment information, thus this simplified model makes it difficult to further meet the control requirements of the actuator, such as actuator rotation angle control and multi-drive coupling control.

B. Contributions

Facing to the limitations of the current research, the contributions of our proposed model and controller are as follows:

1) This work aim to find a more general format for both the electronic and mechanic model in order to reduce the computational complexity without losing accuracy and facilitate the control design. In this paper, we put forward a parameterization of both charge field and strain field to model the real system, which greatly reduces its dimension. The Cosserat rod theory is adopted to deal with the exact nonlinearity in the large deformations of conducting polymer in six degrees of freedom under the interaction with the environment. Comparing with the current modeling methods, our proposed coupling model, with lower dimension and a balance between accuracy, robustness and computational complexity, intent to lay the foundation for real-time simulation and control works.

2) To overcome the problems related to the unknown or imprecise physical parameters, this paper proposes a parameter identification method based on a nonlinear electro-mechanical coupling model. A visual identification system is designed to measure the curvature of actuator which is used for parameter identification.

3) An optimal controller based on the proposed electro-mechanic model is designed in this paper, which lays the foundation work for the subsequent multi-drive coupling trajectory tracking control in the future. Experiments are carried out to validate the controller design and its robustness.

In summary, this paper is organized as follows: A nonlinear modeling of the electronic and mechanical part is introduced in Section II. Then parameter identification is addressed in Section III. Controller design is presented in Section IV. Numerical simulations and experimental validation are presented in Section V. Finally, Section VI concludes this article.

II. Nonlinear model of polymer

The modeling task of conducting polymer can be mainly divided into two parts: the electronic model and the mechanic model. Noting that the working state of IEAP actuator depends on the actuation frequency [20] , it can be classified into two cases: (i). When the actuation frequency is below the mechanical resonance frequency of the actuator, the deformation is quasi-static. (ii). When the actuation frequency is greater than the mechanical resonance frequency, the deformation varies mainly due to inertial mass effects. Thus the dynamics in mechanic model is necessary.

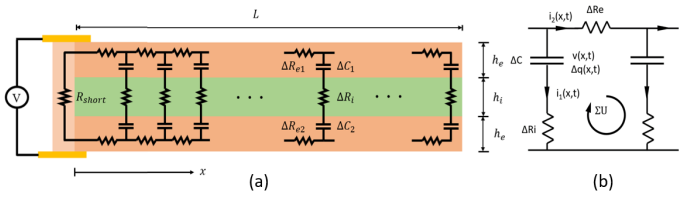

Fig. 1. 2D-RC infinite grid for electronic model.

Based on the above two different cases, this paper investigates different types of models: a nonlinear electronic dynamic model in Section II-A, a mechanic quasi-static model for case (i) and a mechanic dynamic model for case (ii) in Section II-C. The final coupling model is then deduced in Section II-D.

A. Electronic model

In this part we will first build the continuous electronic model which describes the dynamic evolution of charge along actuator. Then the discrete model is built by discretization of the continuous model.

*1) **Strong form of electronic dynamics**:* Denote the total length of polymer as L where two electrode layers outside wrap the middle ion reservoir membrane. When the polymer is charged, the research in [20] shows that the process of charge can be regarded as an infinity RC circuit grid (see Fig. 1(a)). Let us consider an infinitesimal element dx, and denote ΔR_{e1} and ΔR_{e2} as the electric resistance of outer layers and ΔR_i as the ionic resistance of middle layer, ΔC_1 and ΔC_2 as the corresponding capacitances of outer layers, which satisfy the following equations according to its definition:

$$\Delta R_{e1} = \frac{dx}{\omega_{e1} b h_e} \ , \ \Delta R_{e2} = \frac{dx}{\omega_{e2} b h_e} \ , \ \Delta R_i = \frac{h_i}{\omega_i b dx}$$
$$\Delta C_1 = C_{v1} b h_e dx \ , \ \Delta C_2 = C_{v2} b h_e dx,$$

where b represents the width of polymer, h_e is the thickness of the CP layer, C_{v1} and C_{v2} are the volumetric capacitance of

the top CP layer and the bottom CP layer , ω_{e1} and ω_{e2} are the volumetric conductivity of the top CP layer and the under CP layer, ω_i is the volumetric conductivity of the separator layer. For each RC grid element depicted in Fig. 1(a), its scheme can be simplified as Fig. 1(b), where

$$\begin{cases} \Delta R_i = \frac{h_i}{\omega_i b dx} = \frac{r_i}{dx} \\ \Delta R_e = \Delta R_{e1} + \Delta R_{e2} = (\frac{dx}{\omega_{e1} b h_e} + \frac{dx}{\omega_{e2} b h_e})dx = r_e dx \\ \Delta C = \Delta C_1 + \Delta C_2 = (C_{v1} b h_e + C_{v2} b h_e)dx = c_e dx \end{cases} \tag{1}$$

Without loss of generality, it is assumed that the electric resistances and ionic resistance are not constant. In fact, this electronic nonlinear characteristic has been observed in [15], which implies that the values of those resistances depend on the local charge.

As shown in Fig. 1(b), for the RC grid element located at x with dx length, denote v as the voltage of capacity ΔC, Δq as the charge of ΔC, i_1 and i_2 as the currents of the two branches, λ as the linear charge density at x, then v, i_1 and i_2 can be represented by $\lambda(x,t)$ via the following equations:

$$v(x,t) = \frac{\lambda}{c_e},\ i_1(x,t) = \frac{\partial \lambda}{\partial t}dx,\ i_2(x,t) = \int_x^l \frac{\partial \lambda}{\partial t}dr. \tag{2}$$

For each grid as Fig. 1(b), according to Kirchhoff laws (i.e., $\sum U = 0$), we have

$$\begin{aligned} i_2(x,t)\Delta Re + \tfrac{\lambda(x+dx,t)}{c_e} + i_1(x+dx,t)\Delta R_i \\ -i_1(x,t)\Delta R_i - \tfrac{\lambda(x,t)}{c_e} = 0, \end{aligned}$$

With (1) and (2), we can then get the strong form of electronic dynamics from the above equation:

$$r_e(\lambda)\int_x^L \frac{\partial \lambda}{\partial t}dr + \frac{1}{c_e}\frac{\partial \lambda}{\partial x} + r_i(\lambda)\frac{\partial^2 \lambda}{\partial x \partial t} = 0, \tag{3}$$

which is a partial differential equation (PDE) describing the charge density along the polymer, satisfying the following boundary conditions:

$$\lambda(x,0) = 0,\ \frac{\lambda(0,t)}{c_e} + r_i(\lambda(0,t))\frac{\partial \lambda(0,t)}{\partial t} - V_{in} = 0, \tag{4}$$

where V_{in} is the tension input applied on the two CP layers.

Remark 1: Due to the balance of charge in the charging process, the charge along actuator will tend to become stable when time tends to infinity, which means $\frac{\partial \lambda}{\partial t} = 0$, thus $\frac{\partial \lambda}{\partial x} = 0$ according to (3). Consequently, the distribution of charge along actuator at the equilibrium point will become geometrically uniform.

Up to now, we have built the continuous equation of charge density as PDE (3), and with (4) they compose a BVP (Boundary Value Problem). However, analytically solving such a highly nonlinear BVP is quite complicated. In the following, we derive its weak form by applying Galerkin method to approximate the solution via spatially parameterizing the charge field.

*2) **Weak form of electronic dynamics**:* In order to simplify the writing of (3) and (4), we use prime in place of $\frac{\partial}{\partial x}$ and dot in place of $\frac{\partial}{\partial t}$. Thus (3) and (4) can be written as follows:

$$r_e(\lambda)\int_x^L \dot{\lambda}dr + {c_e}^{-1}(\lambda)\lambda' + r_i(\lambda)\dot{\lambda}' = 0, \tag{5}$$

with the boundary condition:

$${c_e}^{-1}(\lambda(0,t))\lambda(0,t) + r_i(\lambda(0,t))\dot{\lambda}(0,t) - V_{in}(t) = 0. \tag{6}$$

Now we can define the "virtual charge displacement" $\delta\lambda$ of each micro RC grid, then the energy balance equation of conducting polymer might be deduced, which corresponds to the weak form of PDE (5) as follows:
$\forall x \in [0,\ L] \mapsto \delta\lambda(x) \in \mathbb{R}$,

$$\int_0^L \delta\lambda^T(x)\left\{r_e\int_x^L \dot{\lambda}dr + {c_e}^{-1}\lambda' + r_i\dot{\lambda}'\right\}dx = 0. \tag{7}$$

*3) **Parameterization charge field**:* Note that the solution of (7) is defined in an infinite set. To discretize the system and find the numerical solution, we consider that the field of charge can be approximated by a set with limited degrees of freedom. To generically handle this kind of approximation, the field of charge λ is defined by the product of basis function and coefficients. i.e.,

$$\lambda(x,t) := \mathbf{\Phi}(x)\boldsymbol{\lambda}(t),\ s \in [0,\ L], \tag{8}$$

where $\mathbf{\Phi}(x) = [\Phi_0,\ \Phi_1, \ldots,\ \Phi_m] \in \mathbb{R}^{1\times m}$ is the basis function and $\boldsymbol{\lambda} = [\lambda_0,\ \lambda_1, \ldots,\ \lambda_m]^T \in \mathbb{R}^{m\times 1}$ is the coefficients. In order to globally parameterize the charge field without losing physical meaning, the basis function $\mathbf{\Phi}(x)$ is chosen by these two assumptions below:

Assumption 1: The conducting polymer can be divided into several sections and for each section the charge density is distributed linearly.

Assumption 2: All the physical parameters are homogeneous in each section.

Based on the piece-wise linear assumption 1, basis function $\mathbf{\Phi}(x)$ holds following structure:

$$\mathbf{\Phi} = \begin{cases} \left[\frac{l-x}{l}, \frac{x}{l}, 0, \ldots, 0\right], & 0 \leqslant x < l \\ \vdots & \vdots \\ \left[0, \ldots, 0, \frac{kl-x}{l}, \frac{x-(k-1)l}{l}, 0, \ldots, 0\right], & (k-1)l \leqslant x < kl \\ \vdots & \vdots \\ \left[0, \ldots, 0, \frac{nl-x}{l}, \frac{x-(n-1)l}{l}\right], & (n-1)l \leqslant x < nl \end{cases}$$

As a result, (8) leads to two relations:

$$\delta\lambda(x) = \mathbf{\Phi}\delta\boldsymbol{\lambda},\ \lambda(x)' = \mathbf{\Phi}'\boldsymbol{\lambda}. \tag{9}$$

*4) **Discrete electronic model**:* Note that the weak form (7) is equivalent to (3). This weak form holds the advantage of realizing the approximation from the continuous dynamics of electronic model to discrete dynamics. Concretely, by substituting (8)-(9) into (7), one can get:

$$\delta\boldsymbol{\lambda}^T\int_0^L \mathbf{\Phi}^T\left\{r_e\int_x^L \mathbf{\Phi}\dot{\boldsymbol{\lambda}}dr + {c_e}^{-1}\mathbf{\Phi}'\boldsymbol{\lambda} + r_i\mathbf{\Phi}'\dot{\boldsymbol{\lambda}}\right\}dx = 0.$$

The equation above should hold for any $\delta\boldsymbol{\lambda}$, thus after removing $\delta\boldsymbol{\lambda}^T$ and adding the boundary condition (6), we obtain the following succinct ODE representation of the electronic model:

$$(\boldsymbol{R_e}\begin{bmatrix}\mathbf{0}\\ \mathbf{P}\end{bmatrix} + \boldsymbol{R_i}\begin{bmatrix}\mathbf{W}\\ \mathbf{Q}\end{bmatrix})\dot{\boldsymbol{\lambda}} + \boldsymbol{C_e}^{-1}\begin{bmatrix}\mathbf{W}\\ \mathbf{Q}\end{bmatrix}\boldsymbol{\lambda} = \begin{bmatrix}V_{in}\\ \mathbf{0}\end{bmatrix}, \tag{10}$$

with

$$\mathbf{W} = \begin{bmatrix}1 & 0 & \dots & 0\end{bmatrix} \in \mathbb{R}^{m+1},$$

$$\boldsymbol{P} = \int_0^L \boldsymbol{\Phi}^T(x) \int_x^L \boldsymbol{\Phi}(r) dr dx, \ \boldsymbol{Q} = \int_0^L \boldsymbol{\Phi}^T(x) \boldsymbol{\Phi}'(x) dx,$$

$$\boldsymbol{R_e} = diag\{r_e(\lambda_0), r_e(\frac{\lambda_0+\lambda_1}{2}), \dots, r_e(\frac{\lambda_{m-1}+\lambda_m}{2})\},$$

$$\boldsymbol{R_i} = diag\{r_i(\lambda_0), r_i(\frac{\lambda_0+\lambda_1}{2}), \dots, r_i(\frac{\lambda_{m-1}+\lambda_m}{2})\},$$

$$\boldsymbol{C_e} = diag\{c_e(\lambda_0), c_e(\frac{\lambda_0+\lambda_1}{2}), \dots, c_e(\frac{\lambda_{m-1}+\lambda_m}{2})\}.$$

After having established the discrete dynamic equation (10) of electronic model to describe the evolution of charge density along actuator, the next step is to show how the charge density of each section can create the deformation of polymer.

B. From electric charge to actuation moment

Consider now one element of 3-layer polymer depicted in Fig. 2 with E_e and E_i being the Young's modulus of the CP layer and the separator layer respectively. Denote α as the strain-to-charge ratio of the CP layers, and λ as the linear charge density of CP layers. Obviously, the values of charge density for these two CP layers should be opposite due to the balance of charge. Thus we define the linear charge density of the upper CP layer as λ, so that of the bottom CP layer should be $-\lambda$. As shown in Fig. 2, for a micro element of the actuator, the stress on its cross section S is comprised with two parts (see Fig. 2): the elastic stress σ_e and the redox stress σ_r. Since the redox strain is proportional with charge density [14], the equivalent redox stress can be calculated as follows:

$$\sigma_r(y) = \begin{cases} -E_e \frac{\alpha\lambda}{bh_e}, & \frac{h_i}{2} < y \leqslant \frac{h_i}{2} + h_e \\ 0, & -\frac{h_i}{2} \leqslant y \leqslant \frac{h_i}{2} \\ E_e \frac{\alpha\lambda}{bh_e}, & -\frac{h_i}{2} - h_e \leqslant y < -\frac{h_i}{2} \end{cases}$$

Consequently, for any cross section we can compute its

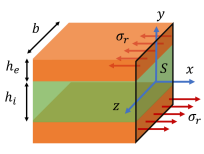

Fig. 2. The equivalent redox stress distribution on the cross section S of polymer based actuator.

actuated force defining in the local frame of cross section. It can be deduced directly that the total contribution of the electric stress is a moment while the forces of the two CP layers counteract with each other:

$$\boldsymbol{\mathcal{F}_a} = \iint_S \boldsymbol{\sigma_r} dS = \boldsymbol{t_1} \iint_S \sigma_r dS = \int \boldsymbol{t_1} \int_{-\frac{h_i}{2}-h_e}^{\frac{h_i}{2}+h_e} \sigma_r dy dz,$$

where vector $\boldsymbol{t_1}$ is the identical direction vector of σ_r (i.e., $\boldsymbol{t_1} = \begin{bmatrix}1 & 0 & 0\end{bmatrix}^T$). The integral part $\int_{-\frac{h_i}{2}-h_e}^{\frac{h_i}{2}+h_e} \sigma_r dy = 0$, which yields $\boldsymbol{\mathcal{F}_a} = \begin{bmatrix}0 & 0 & 0\end{bmatrix}^T$,

$$\begin{aligned} \boldsymbol{\mathcal{M}_a} &= \iint_S \boldsymbol{y} \times \boldsymbol{\sigma_r} dS = \iint_S \boldsymbol{t_2} \times \boldsymbol{t_1} \sigma_r y dS \\ &= \int_0^b \boldsymbol{t} \int_{-\frac{h_i}{2}-h_e}^{\frac{h_i}{2}+h_e} \sigma_r y dy dz = \boldsymbol{t} \int_0^b \frac{E_e \alpha (h_e+h_i)\lambda}{b} dz \\ &= \boldsymbol{t} E_e \alpha (h_e+h_i)\lambda = \boldsymbol{t}\beta\lambda = \begin{bmatrix}0 & 0 & \beta\lambda\end{bmatrix}^T, \end{aligned} \tag{11}$$

where $\boldsymbol{t_2}$ is the identical direction vector of $\boldsymbol{y}$ (i.e., $\boldsymbol{t_2} = \begin{bmatrix}0 & 1 & 0\end{bmatrix}^T$), $\boldsymbol{t} = \boldsymbol{t_2} \times \boldsymbol{t_1} = \begin{bmatrix}0 & 0 & -1\end{bmatrix}^T$, $\beta = E_e\alpha(h_e + h_i)\lambda$. For ease of expression, we use an actuation wrench $\boldsymbol{\Lambda}_a \in \mathbb{R}^6$ to represent $\boldsymbol{\mathcal{F}_a}$ and $\boldsymbol{\mathcal{M}_a}$:

$$\boldsymbol{\Lambda}_a = \begin{bmatrix}\boldsymbol{\mathcal{M}_a}^T & \boldsymbol{\mathcal{F}_a}^T\end{bmatrix}^T = \begin{bmatrix}0 & 0 & \beta\lambda & 0 & 0 & 0\end{bmatrix} = \Gamma\beta\lambda \tag{12}$$

where $\Gamma = \begin{bmatrix}0 & 0 & 1 & 0 & 0 & 0\end{bmatrix}^T$.

Once we deduced the actuation moment of polymer actuator, the dynamic state of polymer actuator can be then analyzed.

C. Mechanic model

In the aspect of mechanic analysis, it is natural that the polymer actuator can be regarded as a slender beam. The local charge accumulated inside the polymer will induce the internal stress which causes the deformation of the polymer actuator. In this section we will first build the relation between the internal force and local charge. Then the dynamics of the polymer actuator will be analyzed in the following subsections, where we consider the deformation of polymer actuator in 6 DOF (bending, shear, torsion, extension) under actuation force and external force.

*1) **Continuous geometries & kinematics of Cosserat rod**:* In cosserat rod theory, the configuration of rod is described by the rotation matrix $\boldsymbol{R} \in \mathrm{SO}(3)$ and position vector $\mathbf{u} \in \mathbb{R}^3$, which represent the orientation and position of each cross section of the rod with respect to global frame. Thus, the configuration space of rod is defined as follows:

$$\mathcal{C} = \{\boldsymbol{g} : x \in [0, L] \mapsto \boldsymbol{g}(s) \in \mathrm{SE}(3)\}, \ \boldsymbol{g} = \begin{bmatrix}\boldsymbol{R} & \boldsymbol{u} \\ \mathbf{0}^T & 1\end{bmatrix}$$

The space-time variation of the configuration can be defined with two vector fields $\boldsymbol{\xi}$ and $\boldsymbol{\eta}$ which stand for the strain and velocity of rod respectively in local frame: $\forall x \in [0, L] \mapsto \widehat{\boldsymbol{\xi}}(x) \in \mathrm{se}(3)$:

$$\widehat{\boldsymbol{\xi}} = \boldsymbol{g}^{-1}\boldsymbol{g}' = \begin{bmatrix}\tilde{\boldsymbol{\kappa}} & \boldsymbol{\epsilon} \\ \mathbf{0}^T & 0\end{bmatrix} \in \mathrm{se}(3), \ \boldsymbol{\xi} = \widehat{\boldsymbol{\xi}}^\vee = \begin{bmatrix}\boldsymbol{\kappa}^T & \boldsymbol{\epsilon}^T\end{bmatrix}^T \in \mathbb{R}^6$$

where $\boldsymbol{\kappa}$ stands for the angular strain and $\boldsymbol{\epsilon}$ represents the linear strain. $\forall x \in [0, L] \mapsto \widehat{\boldsymbol{\eta}}(s) \in \mathrm{se}(3)$:

$$\widehat{\boldsymbol{\eta}} = \boldsymbol{g}^{-1}\dot{\boldsymbol{g}} = \begin{bmatrix}\tilde{\boldsymbol{w}} & \boldsymbol{v} \\ \mathbf{0}^T & 0\end{bmatrix} \in \mathrm{se}(3), \ \boldsymbol{\eta} = \widehat{\boldsymbol{\eta}}^\vee = \begin{bmatrix}\boldsymbol{w}^T & \boldsymbol{v}^T\end{bmatrix}^T \in \mathbb{R}^6$$

where $\boldsymbol{w}$ stands for the angular velocity and $\boldsymbol{v}$ represents the linear velocity with respect of local frame.

Based on the definitions of $\boldsymbol{\xi}$ and $\boldsymbol{\eta}$, one can derive the geometries and kinematics through the following two equations respectively:

$$\boldsymbol{g}' = \boldsymbol{g}\widehat{\boldsymbol{\xi}}\ ,\ \boldsymbol{\eta}' = \dot{\boldsymbol{\xi}} - \mathrm{ad}_{\boldsymbol{\xi}}\,\boldsymbol{\eta} \tag{13}$$

which connect the velocity and acceleration with strain.

*2) **Strong form of dynamics**:* To analyze the mechanic behavior of beam such as polymer actuator, the strong form of dynamic model can be demonstrated as (14), which is detailed in [21] and [22]:

$$\boldsymbol{\mathcal{M}}\dot{\boldsymbol{\eta}} - ad_{\boldsymbol{\eta}}^T\boldsymbol{\mathcal{M}}\boldsymbol{\eta} = \boldsymbol{\Lambda}_i' - \mathrm{ad}_{\boldsymbol{\xi}}^T\,\boldsymbol{\Lambda}_i - \boldsymbol{\Lambda}_a' + \mathrm{ad}_{\boldsymbol{\xi}}^T\,\boldsymbol{\Lambda}_a + \overline{\boldsymbol{\Lambda}}_e, \tag{14}$$

satisfying the following boundary conditions:

$$\boldsymbol{\Lambda}_i(L) - \boldsymbol{\Lambda}_a(L) = \boldsymbol{\Lambda}_e(L), \tag{15}$$

where $\mathcal{M}$ represents the screw inertia matrix, $\mathcal{M} = diag\{\rho I_x, \rho I_y, \rho I_z, \rho A, \rho A, \rho A\} \in \mathbb{R}^{6\times 6}$. ρ is the equivalent mass density of the total actuator. A is the area of cross-section. I_x, I_y and I_z are the second moment of the area of the three axis respectively. $\boldsymbol{\Lambda}_i \in \mathbb{R}^6$ represents the internal force wrench of polymer actuator which can be calculated by the constitutive equation based on Cosserat model hypotheses: $\boldsymbol{\Lambda}_i = \mathcal{K}\boldsymbol{\xi}$ with $\mathcal{K} = diag\{GI_x, EI_y, EI_z, EA, GA, GA\} \in \mathbb{R}^{6\times 6}$, the equivalent stiffness matrix of the entire electrodes plus polymer layers, where G represents the shear modulus and E represents the young's modulus. $\boldsymbol{\Lambda}_a \in \mathbb{R}^6$ represents the actuation force wrench of polymer actuator. $\overline{\boldsymbol{\Lambda}}_e \in \mathbb{R}^6$ represents the distributed load applied on the polymer actuator.

*3) **Weak form of dynamics**:* According to the Lagrange–d'Alembert principle, if we define the virtual displacement of each micro solid along polymer actuator $\delta\boldsymbol{r}(x)$, one can write the virtual work of polymer actuator which leads to the weak form of equation (14) as follows:
$\forall x \in [0,\ L] \mapsto \delta\boldsymbol{r}(x) \in \mathbb{R}^6$,

$$\begin{aligned}\int_0^L \delta\boldsymbol{r}^T(x)(&\boldsymbol{\mathcal{M}}\dot{\boldsymbol{\eta}} - ad_{\boldsymbol{\eta}}^T\boldsymbol{\mathcal{M}}\boldsymbol{\eta} \\ &- \boldsymbol{\Lambda}_i' + \mathrm{ad}_{\boldsymbol{\xi}}^T\,\boldsymbol{\Lambda}_i + \boldsymbol{\Lambda}_a' - \mathrm{ad}_{\boldsymbol{\xi}}^T\,\boldsymbol{\Lambda}_a - \overline{\boldsymbol{\Lambda}}_e)ds = 0\end{aligned} \tag{16}$$

*4) **Parameterization strain field**:* To find the solution of equation (16), the same parameterization idea with electric model is introduced here in order to get the discretize the mechanic model. (13) represents the geometries of the rod. i.e., its configuration space can be reconstructed by knowing the strain $\boldsymbol{\xi}$ and the initial condition $\boldsymbol{g}(0)$. As a result, this yields to the second definition of the configuration space: $\mathcal{C} = \mathrm{SE}(3) \times \mathbb{S}$, where $\mathbb{S} = \{\boldsymbol{\xi} : x \in [0, L] \mapsto \boldsymbol{\xi} \in \mathbb{R}^6\}$. Note that space $\mathbb{S}$ is an infinite dimensional space. For the sake of approximating the solution of (16), we consider that a finite dimensional space $\mathbb{S}$ can be adopted by parameterizing the strain field $\boldsymbol{\xi}$, i.e.,

$$\boldsymbol{\xi}(s) := \boldsymbol{\xi}_0 + \boldsymbol{\Psi}(x)\boldsymbol{q},\ x \in [0,\ L], \tag{17}$$

where $\boldsymbol{\Psi}(x) = [\Psi_0,\ \Psi_1, \ldots,\ \Psi_n] \in \mathbb{R}^{6\times n}$ is the basis function and $\boldsymbol{q} = [\boldsymbol{\xi}_0,\ \boldsymbol{\xi}_1, \ldots,\ \boldsymbol{\xi}_n]^T \in \mathbb{R}^{n\times 1}$ is the coefficients. $\boldsymbol{\xi}_0$ stands the constant part of $\boldsymbol{\xi}$ which we do not want to chose to be variable.

*5) **Discrete mechanic model**:* As a result of parameterization of strain field, the geometries and kinematics can be analytically reconstructed by $\boldsymbol{q}$ from (13). For instance, if we chose $\boldsymbol{\Psi}(x)$ as a piecewise constant basis function, the analytical solutions of configuration $\boldsymbol{g}$ and $\boldsymbol{\eta}$ are as follows: for $x \in [l_{i-1},\ l_i]$,

$$\boldsymbol{g}(x,t) = \boldsymbol{g}(l_{i-1},t)e^{\boldsymbol{\xi}_i(x-l_{i-1})}, \tag{18}$$

$$\begin{aligned}\boldsymbol{\eta}(x,t) =& e^{-(x-l_{i-1})\,\mathrm{ad}_{\boldsymbol{\xi}_i}} \\ &\left(\boldsymbol{\eta}(l_{i-1},t) + \int_{l_{i-1}}^{x} e^{(s-l_{i-1})\,\mathrm{ad}_{\boldsymbol{\xi}_i}} ds\dot{\boldsymbol{\xi}}_i\right).\end{aligned} \tag{19}$$

Thanks to the work of [23], these mapping between $\boldsymbol{\xi}$ and $\boldsymbol{\eta}$ can be represented by the Jacobian matrix $\boldsymbol{J}(x,\boldsymbol{q})$:

$$\boldsymbol{\eta}(x,t) = \boldsymbol{J}(x,\boldsymbol{q})\dot{\boldsymbol{q}}(t). \tag{20}$$

Furthermore, the relationship of their time derivative can be deduced by the derivation of (20):

$$\dot{\boldsymbol{\eta}}(x,t) = \dot{\boldsymbol{J}}(x,\boldsymbol{q},\dot{\boldsymbol{q}})\dot{\boldsymbol{q}}(t) + \boldsymbol{J}(x,\boldsymbol{q})\ddot{\boldsymbol{q}}(t). \tag{21}$$

From (20) one can deduce $\delta\boldsymbol{r}(x) = \boldsymbol{J}(x)\delta\boldsymbol{q}$. Taking it into equation (16) yields:

$$\begin{aligned}\delta\boldsymbol{q}^T\int_0^L \boldsymbol{J}^T(&\boldsymbol{\mathcal{M}}\dot{\boldsymbol{\eta}} - ad_{\boldsymbol{\eta}}^T\boldsymbol{\mathcal{M}}\boldsymbol{\eta} - \boldsymbol{\Lambda}_i' + \mathrm{ad}_{\boldsymbol{\xi}}^T\,\boldsymbol{\Lambda}_i \\ &+ \boldsymbol{\Lambda}_a' - \mathrm{ad}_{\boldsymbol{\xi}}^T\,\boldsymbol{\Lambda}_a - \overline{\boldsymbol{\Lambda}}_e)ds = 0.\end{aligned} \tag{22}$$

After removing $\delta\boldsymbol{q}$ and taking (20) (21) into (22), we can finally get the discrete dynamic equation:

$$\boldsymbol{M}(\boldsymbol{q})\ddot{\boldsymbol{q}} + \boldsymbol{C}(\boldsymbol{q},\dot{\boldsymbol{q}})\dot{\boldsymbol{q}} = \boldsymbol{F_i}(\boldsymbol{q}) + \boldsymbol{F_a}(\boldsymbol{q}) + \boldsymbol{F_e}(\boldsymbol{q}) + \boldsymbol{N}(\boldsymbol{q})\mathcal{G} \tag{23}$$

where $\boldsymbol{F_e}(\boldsymbol{q}) = \int_0^L \boldsymbol{J}^T\overline{\boldsymbol{\Lambda}}_e ds,\ \boldsymbol{N}(\boldsymbol{q}) = \int_0^L \boldsymbol{J}^T\mathcal{M}\mathrm{Ad}_{\boldsymbol{g}}^{-1}ds,\ \mathcal{G} = [\boldsymbol{0}_{1\times 4}\ 9.81\ 0]^T$ is the twist of gravitational acceleration,

$$\boldsymbol{F_i} = \int_0^L \boldsymbol{J}^T(\boldsymbol{\Lambda}_i' - \mathrm{ad}_{\boldsymbol{\xi}}^T\,\boldsymbol{\Lambda}_i)ds,\ \boldsymbol{F_a} = -\int_0^L \boldsymbol{J}^T(\boldsymbol{\Lambda}_a' - \mathrm{ad}_{\boldsymbol{\xi}}^T\,\boldsymbol{\Lambda}_a)ds. \tag{24}$$

Form kinematics in (13) one can get $\boldsymbol{\eta}' = -\,\mathrm{ad}_{\boldsymbol{\xi}_i}\,\boldsymbol{\eta} + \dot{\boldsymbol{\xi}}_i$ for $x \in [l_{i-1},\ l_i]$. Taking (20) into the above equation yields:

$$\boldsymbol{J}'\dot{\boldsymbol{q}} = -\,\mathrm{ad}_{\boldsymbol{\xi}_i}\,\boldsymbol{J}\dot{\boldsymbol{q}} + \dot{\boldsymbol{\xi}}_i = -\,\mathrm{ad}_{\boldsymbol{\xi}_i}\,\boldsymbol{J}\dot{\boldsymbol{q}} + \boldsymbol{\Psi}\dot{\boldsymbol{q}}.$$

Thus, one can get $\boldsymbol{J}' = -\,\mathrm{ad}_{\boldsymbol{\xi}_i}\,\boldsymbol{J} + \boldsymbol{\Psi}$. Then, by substituting this relationship into $\boldsymbol{F_i}$ in (24) and using the integral by parts one can obtain

$$\begin{aligned}\boldsymbol{F_i} &= \int_0^L (\boldsymbol{J}^T\boldsymbol{\Lambda}_i)' - (-\,\mathrm{ad}_{\boldsymbol{\xi}}\,\boldsymbol{J} + \boldsymbol{\Psi})^T\boldsymbol{\Lambda}_i - \boldsymbol{J}^T\,\mathrm{ad}_{\boldsymbol{\xi}}^T\,\boldsymbol{\Lambda}_i ds \\ &= \int_0^L (\boldsymbol{J}^T\boldsymbol{\Lambda}_i)' - \boldsymbol{\Psi}^T\boldsymbol{\Lambda}_i ds = \boldsymbol{J}^T\boldsymbol{\Lambda}_i|_0^L - \int_0^L \boldsymbol{\Psi}^T\boldsymbol{\Lambda}_i ds.\end{aligned}$$

The two boundary conditions $\boldsymbol{J}(0) = \boldsymbol{0}$ and $\boldsymbol{\Lambda}_i(L) = \boldsymbol{\Lambda}_a(L)$ lead to $\boldsymbol{J}^T\boldsymbol{\Lambda}_i|_0^L = \boldsymbol{J}^T(L)\boldsymbol{\Lambda}_a(L)$. The piecewise constant strain assumption leads to $\Lambda_i = \mathcal{K}\boldsymbol{\xi} = \mathcal{K}\boldsymbol{\Psi}\boldsymbol{q}$. As a result, $\boldsymbol{F_i}$ can be simplified by substituting these two relations into the equation above: $\boldsymbol{F_i} = \boldsymbol{J}^T(L)\boldsymbol{\Lambda}_a(L) - \int_0^L \boldsymbol{\Psi}^T\mathcal{K}\boldsymbol{\Psi}ds\boldsymbol{q}$. Thanks to the same mathematical form of $\boldsymbol{F_a}$ and $\boldsymbol{F_i}$, the same structure holds: $\boldsymbol{F_a} = -\boldsymbol{J}^T(L)\boldsymbol{\Lambda}_a(L) + \int_0^L \boldsymbol{\Psi}^T\Gamma\boldsymbol{\Phi}ds\beta\boldsymbol{\lambda}$. After deducing $\boldsymbol{F_i}$ and $\boldsymbol{F_a}$, the final mechanic model can be rewritten as following:

$$\boldsymbol{M}\ddot{\boldsymbol{q}} + \boldsymbol{C}\dot{\boldsymbol{q}} + \boldsymbol{K}\boldsymbol{q} = \boldsymbol{H}\boldsymbol{z}(t) + \boldsymbol{P}, \tag{25}$$

with the following definitions of all matrices:

- $\boldsymbol{z}(t) = [z_0,\ z_1, \dots,\ z_m]^T = \beta\boldsymbol{\lambda}(t) \in \mathbb{R}^m$, the actuation input;
- $\boldsymbol{M}(\boldsymbol{q}) = \int_0^L \boldsymbol{J}^T\boldsymbol{\mathcal{M}}\boldsymbol{J}ds \in \mathbb{R}^{n\times n}$, the mass matrix;
- $\boldsymbol{C}(\boldsymbol{q},\dot{\boldsymbol{q}}) = \int_0^L \boldsymbol{J}^T(\boldsymbol{\mathcal{M}}\dot{\boldsymbol{J}} - ad^T_{\boldsymbol{J}\dot{\boldsymbol{q}}}\boldsymbol{\mathcal{M}}\boldsymbol{J})ds \in \mathbb{R}^{n\times n}$, the Coriolis matrix;
- $\boldsymbol{K} = \int_0^L \boldsymbol{\Psi}^T\mathcal{K}\boldsymbol{\Psi}ds \in \mathbb{R}^{n\times n}$, the stiffness matrix;
- $\boldsymbol{H} = \int_0^L \boldsymbol{\Psi}^T\Gamma\boldsymbol{\Phi}ds \in \mathbb{R}^{n\times m}$, the actuation matrix;
- $\boldsymbol{P}(\boldsymbol{q},t) = \boldsymbol{F_e}(\boldsymbol{q},t) + \boldsymbol{N}(\boldsymbol{q})\mathcal{G} \in \mathbb{R}^n$, the contribution of external force and gravity.

D. Whole coupling model

After having deduced the electric model and the mechanical model of polymer, we can then gather these two models together to describe the whole dynamics of input tension and the corresponding deformation by the combination of the deduced electric system:

$$(\boldsymbol{Q_1}\boldsymbol{\Sigma_1} + \boldsymbol{Q_2}\boldsymbol{\Sigma_2})\dot{\boldsymbol{z}} + \boldsymbol{Q_3}\boldsymbol{\Sigma_2}\boldsymbol{z} = \boldsymbol{U}V_{in}, \tag{26}$$

with

$$\boldsymbol{Q_1} = \frac{1}{\beta}\boldsymbol{R_e},\ \boldsymbol{Q_2} = \frac{1}{\beta}\boldsymbol{R_i},\ \boldsymbol{Q_3} = \frac{1}{\beta}\boldsymbol{C_e}^{-1},$$

$$\boldsymbol{\Sigma_1} = \begin{bmatrix}\mathbf{0}\\ \mathbf{P}\end{bmatrix},\ \boldsymbol{\Sigma_2} = \begin{bmatrix}\mathbf{W}\\ \mathbf{Q}\end{bmatrix},\ \boldsymbol{U} = \begin{bmatrix}\mathbf{1}\\ \mathbf{0}\end{bmatrix},$$

and the obtained mechanic system:

$$\boldsymbol{M}\ddot{\boldsymbol{q}} + \boldsymbol{C}\dot{\boldsymbol{q}} + \boldsymbol{K}\boldsymbol{q} = \boldsymbol{H}\boldsymbol{z}(t) + \boldsymbol{P}. \tag{27}$$

If the actuator works in quasi-static state, one can obtain its static model by just deleting the first two items $\boldsymbol{M}\ddot{\boldsymbol{q}}$ and $\boldsymbol{C}\dot{\boldsymbol{q}}$ of (27).

III. Parameters identification

In the case of polymer actuator, the parameters of electric system are normally hard to measure directly, thus an identification work is necessary via which we can estimate the parameters from the data that are easily to measure. The electric model (26) deduced in the above section is nonlinear and contains unknown matrix $\boldsymbol{Q_1}$, $\boldsymbol{Q_2}$, $\boldsymbol{Q_3}$ which are nonlinear function of $\boldsymbol{z}$. Therefore, a parameter identification procedure is presented in this section to reveal the nonlinearlity of those parameters.

From the definition of $\boldsymbol{R_e}$, $\boldsymbol{R_i}$ and $\boldsymbol{C_e}$, we define:

$$\boldsymbol{Q_1} = diag\{q_1(z_0), q_1(\frac{z_0+z_1}{2}), q_1(\frac{z_1+z_2}{2}), \dots, q_1(\frac{z_{m-1}+z_m}{2})\},$$

$$\boldsymbol{Q_2} = diag\{q_2(z_0), q_2(\frac{z_0+z_1}{2}), q_2(\frac{z_1+z_2}{2}), \dots, q_2(\frac{z_{m-1}+z_m}{2})\},$$

$$\boldsymbol{Q_3} = diag\{q_3(z_0), q_3(\frac{z_0+z_1}{2}), q_3(\frac{z_1+z_2}{2}), \dots, q_3(\frac{z_{m-1}+z_m}{2})\}.$$

It is assumed that these nonlinearlities of function q can be approximated by polynomials with certain order k, i.e.,

$$q_1(s) = \sum_{i=0}^{k} a_i s^i\ ,\ q_2(s) = \sum_{i=0}^{k} b_i s^i\ ,\ q_3(s) = \sum_{i=0}^{k} c_i s^i. \tag{28}$$

By noting $\boldsymbol{a} = [a_0, \dots, a_k]$, $\boldsymbol{b} = [b_0, \dots, b_k]$, $\boldsymbol{c} = [c_0, \dots, c_k]$ and $\boldsymbol{\Pi} = [\boldsymbol{I}\quad diag(\boldsymbol{z})\quad diag^2(\boldsymbol{z})\quad \dots\quad diag^k(\boldsymbol{z})]$, the matrix $\boldsymbol{Q_1}$, $\boldsymbol{Q_2}$ and $\boldsymbol{Q_3}$ can be represented as: $\boldsymbol{Q_1} = \boldsymbol{\Pi}\boldsymbol{a}^T, \boldsymbol{Q_2} = \boldsymbol{\Pi}\boldsymbol{b}^T, \boldsymbol{Q_3} = \boldsymbol{\Pi}\boldsymbol{c}^T$. Set $\boldsymbol{\theta} = [\boldsymbol{a}\quad \boldsymbol{b}\quad \boldsymbol{c}]^T$ and concatenate the following values at different time from t_1 to t_{n_p} with $n_p > m$ where m is the dimension of $\boldsymbol{z}$:

$$\boldsymbol{\Xi} = \begin{bmatrix} \boldsymbol{\Sigma_1}\boldsymbol{\Pi}(t_1)\dot{\boldsymbol{z}}(t_1) & \boldsymbol{\Sigma_2}\boldsymbol{\Pi}(t_1)\dot{\boldsymbol{z}}(t_1) & \boldsymbol{\Sigma_2}\boldsymbol{\Pi}(t_1)\boldsymbol{z}(t_1) \\ \vdots & \vdots & \vdots \\ \boldsymbol{\Sigma_1}\boldsymbol{\Pi}(t_{n_p})\dot{\boldsymbol{z}}(t_{n_p}) & \boldsymbol{\Sigma_2}\boldsymbol{\Pi}(t_{n_p})\dot{\boldsymbol{z}}(t_{n_p}) & \boldsymbol{\Sigma_2}\boldsymbol{\Pi}(t_{n_p})\boldsymbol{z}(t_{n_p}) \end{bmatrix}$$

System (26) can be written into the following algebraic form: $\boldsymbol{\Xi}\boldsymbol{\theta} = \boldsymbol{\Psi}$, where $\boldsymbol{\Psi} = [\boldsymbol{U}^T V_{in}(t_1),\quad \cdots,\quad \boldsymbol{U}^T V_{in}(t_{n_p})]^T$. It is clear that, if all the $\boldsymbol{z}$ can be measurable and $\boldsymbol{\Xi}$ is full row rank, then $\boldsymbol{\theta}$ can be identified by using classical least square method.

IV. Controller design

This section is devoted to designing controller to control the orientation of polymer at free state, as depicted in Fig. 3.

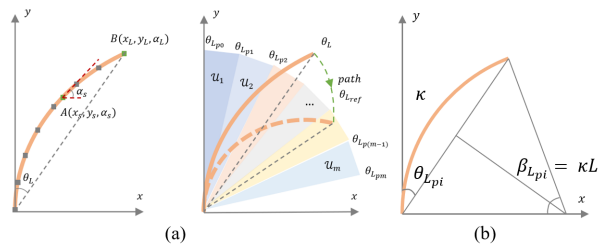

Fig. 3. (a). Geometry of polymer based actuator and its linearization in workspace. α_s is the tangent angle of point A; θ_L is the included angle between vector of end point and axis y; $\theta_{L_{ref}}$ is the reference angle; the figure on right side shows the linearization of system in workspace. (b). Geometry at $\theta_{L_{p_i}}$ when the curvature of actuator is uniform.

A. State-space representation

In our study, the actuation frequency is below the mechanical resonance frequency of the actuator, thus only quasi-static model is considered in the experimental tests. From (27) one can then get the mechanic system of quasi-static model ignoring the gravity and external force:

$$\boldsymbol{K}\boldsymbol{q} = -\boldsymbol{H}\boldsymbol{z}(t). \tag{29}$$

It is clear that in this scene there is only one variable degree of freedom which is the angular strain κ along axis z. Thus here we firstly reduce the order of (29) by a matrix $\boldsymbol{B} = [\mathbf{0}_{1\times 2}\ 1\ \mathbf{0}_{1\times 3}]$:

$$\kappa = -\boldsymbol{B}\boldsymbol{K}^{-1}\boldsymbol{H}\boldsymbol{z}. \tag{30}$$

From κ one can calculate the geometric matrix $\boldsymbol{g}$ by (18) and extract the position of end-effector and its orientation from $\boldsymbol{g}$:

$$\boldsymbol{p} = \boldsymbol{D}\boldsymbol{g}(\kappa)\boldsymbol{T}, \tag{31}$$

with $\boldsymbol{D} = [\mathbf{I}_{3\times 3}\quad \mathbf{0}]$, $\boldsymbol{T} = [0\quad 0\quad 0\quad 1]^T$. As a result, the bending θ_L can be deduced by $\boldsymbol{p}$:

$$\theta_L = \arctan(\boldsymbol{p}). \tag{32}$$

Consider the deduced system (26) (30) (31) and (32), it can be written into the following state-space form:

$$\begin{cases} \dot{\boldsymbol{z}} = \boldsymbol{f}(\boldsymbol{z}) + \boldsymbol{g}(\boldsymbol{z})u(t) \\ \theta_L = h(\boldsymbol{z}) \end{cases} \tag{33}$$

where $\boldsymbol{f}(\boldsymbol{z}) = -(\boldsymbol{Q_1\Sigma_1} + \boldsymbol{Q_2\Sigma_2})^{-1}\boldsymbol{Q_3\Sigma_2 z}$, $\boldsymbol{g}(\boldsymbol{z}) = (\boldsymbol{Q_1\Sigma_1} + \boldsymbol{Q_2\Sigma_2})^{-1}\boldsymbol{U}$, $u(t) = V_{in}(t)$ and function $h(\boldsymbol{z})$ is implicitly defined by (30) (31) and (32).

B. Observer design

In the aspect of control, considering the different application scenarios of polymer actuator, we suppose that one can only measure the position of end effector, thus in order to design state-feedback controller to control θ_L, we need to design firstly an observer to estimate $\boldsymbol{z}$. Considering that the system is nonlinear and observable, extended Kalman filter [24] has been adopted in this paper, whose form is written as

$$\dot{\hat{\boldsymbol{z}}} = \boldsymbol{f}(\hat{\boldsymbol{z}}) + \boldsymbol{g}(\hat{\boldsymbol{z}})u + \boldsymbol{P}\boldsymbol{H}^T\boldsymbol{R}^{-1}[\theta_L - h(\boldsymbol{z})], \tag{34}$$

with $\boldsymbol{P}$ is the solution of the following equation:

$$\dot{\boldsymbol{P}} = \boldsymbol{A}\boldsymbol{P} + \boldsymbol{P}\boldsymbol{A}^T + \boldsymbol{Q} - \boldsymbol{P}\boldsymbol{H}^T\boldsymbol{R}^{-1}\boldsymbol{H}\boldsymbol{P},$$

where $\boldsymbol{A} = \frac{\partial \boldsymbol{f}}{\partial \boldsymbol{z}}|_{\boldsymbol{z}=\hat{\boldsymbol{z}}}, \boldsymbol{H} = \frac{\partial \boldsymbol{h}}{\partial \boldsymbol{z}}|_{\boldsymbol{z}=\hat{\boldsymbol{z}}}$. matrix $\boldsymbol{Q}$ and $\boldsymbol{R}$ are respectively the power spectral density of process noise and that of the observation noise, which represent the errors of system and measurement respectively.

C. Interpolation and linearization

As shown in Fig. 3(a), for the end-effector of polymer, we firstly divide the workspace between $\theta_{L_{min}}$ and $\theta_{L_{max}}$ by $m+1$ points $\theta_{L_{p_i}}$ to form m zones $\mathcal{U}_i = [\theta_{L_{p_{i-1}}}, \theta_{L_{p_i}}]$ with $\theta_{L_{p_0}} = \theta_{L_{min}}$ and $\theta_{L_{p_m}} = \theta_{L_{max}}$, i.e., $[\theta_{L_{min}}, \theta_{L_{max}}] = \cup_{i=1}^{m}\mathcal{U}_i$. Then the reference path $\theta_{L_{ref}}(t)$ is interpolated by $\theta_{L_{p_i}}$, and nonlinear system (33) whose output is located into the ith zone $\mathcal{U}_i$ is linearized at the equilibrium point $\theta_{L_{p_i}}$, based on which linear controller will be designed to drive θ_L moving toward reference $\theta_{L_{ref}}$.

According to Remark 1 in Section II, the equilibrium charge density λ for a given orientation $\theta_{L_{p_i}}$ is geometrically uniform. Thus, for any $\theta_{L_{p_i}} \in [\theta_{L_{min}}, \theta_{L_{max}}]$ we have $z_0(\theta_{L_{p_i}}, \infty) = \cdots = z_n(\theta_{L_{p_i}}, \infty)$. As shown in Fig. 3(b), the geometry leads to the following relation:

$$\kappa(\theta_{L_{p_i}}, \infty) = \frac{\beta_{L_{p_i}}}{L} = \frac{2\theta_{L_{p_i}}}{L}, \forall \theta_{L_{p_i}} \in [\theta_{L_{min}}, \theta_{L_{max}}]. \tag{35}$$

Thus one can deduce $z(\theta_{L_{p_i}}, \infty)$ from (30):

$$z_0(\theta_{L_{p_i}}, \infty) = \cdots = z_n(\theta_{L_{p_i}}, \infty) = EI_z\kappa(\theta_{L_{p_i}}, \infty).$$

For simplicity, at each $\theta_{L_{p_i}} \in [\theta_{L_{min}}, \theta_{L_{max}}]$, note the equilibrium $\boldsymbol{z}$ as $\boldsymbol{z_{eq}}(\theta_{L_{p_i}}) = \left[z_0(\theta_{L_{p_i}}, \infty), \cdots, z_n(\theta_{L_{p_i}}, \infty)\right]^T$. By taking $\boldsymbol{z_{eq}}(\theta_{L_{p_i}})$ in (33), the input voltage u_{eq} of equilibrium point can be solved.

Such a linearization of nonlinear system (33) at $\theta_{L_{p_i}}$ yields

$$\begin{cases} \dot{\boldsymbol{z}} = \boldsymbol{A}_{\boldsymbol{z_{eq}}(\theta_{L_{p_i}})}(\boldsymbol{z} - \boldsymbol{z_{eq}}(\theta_{L_{p_i}})) \\ \qquad\qquad + \boldsymbol{B}_{\boldsymbol{z_{eq}}(\theta_{L_{p_i}})}(u - u_{eq}(\theta_{L_{p_i}})) \quad , \forall \theta_{L_{p_i}} \in \mathcal{U}_i \\ \theta_L = \boldsymbol{H}_{\boldsymbol{z_{eq}}(\theta_{L_{p_i}})}(\boldsymbol{z} - \boldsymbol{z_{eq}}(\theta_{L_{p_i}})) + \theta_{L_{p_i}} \end{cases} \tag{36}$$

where

$$\begin{cases} \boldsymbol{A}_{\boldsymbol{z_{eq}}(\theta_{L_{p_i}})} = \frac{\partial \boldsymbol{f}}{\partial \boldsymbol{z}}|_{\boldsymbol{z}=\boldsymbol{z_{eq}}(\theta_{L_{p_i}})}, \boldsymbol{B}_{\boldsymbol{z_{eq}}(\theta_{L_{p_i}})} = \frac{\partial \boldsymbol{g}}{\partial \boldsymbol{z}}|_{\boldsymbol{z}=\boldsymbol{z_{eq}}(\theta_{L_{p_i}})} \\ \boldsymbol{H}_{\boldsymbol{z_{eq}}(\theta_{L_{p_i}})} = \frac{\partial h}{\partial \boldsymbol{z}}|_{\boldsymbol{z}=\boldsymbol{z_{eq}}(\theta_{L_{p_i}})} \end{cases} \tag{37}$$

D. Controller design

The above linearized system can be represented by tracking error with extended state below:

$$\boldsymbol{x} = \begin{bmatrix} \boldsymbol{e_z}^T & e_{i\theta} \end{bmatrix}^T,$$

where $\boldsymbol{e_z} = \boldsymbol{z_{eq}}(\theta_{L_{p_i}}) - \boldsymbol{z}$, $e_\theta = \theta_{L_{p_i}} - \theta_L$ and $e_{i\theta} = \int e_\theta dt$. With the above state, we can obtain the following observation error dynamics:

$$\begin{aligned} \begin{bmatrix} \dot{\boldsymbol{e}}_{\boldsymbol{z}} \\ \dot{e}_{i\theta} \end{bmatrix} &= \underbrace{\begin{bmatrix} \boldsymbol{A}_{\boldsymbol{z_{eq}}(\theta_{L_{p_i}})} & \boldsymbol{0} \\ \boldsymbol{H}_{\boldsymbol{z_{eq}}(\theta_{L_{p_i}})} & 0 \end{bmatrix}}_{\bar{\boldsymbol{A}}} \begin{bmatrix} \boldsymbol{e_z} \\ e_{i\theta} \end{bmatrix} \\ &+ \underbrace{\begin{bmatrix} -\boldsymbol{B}_{\boldsymbol{z_{eq}}(\theta_{L_{p_i}})} \\ 0 \end{bmatrix}}_{\bar{\boldsymbol{B}}} \underbrace{(u - u_{eq}(\theta_{L_{p_i}}))}_{\bar{u}}. \end{aligned} \tag{38}$$

Remark 2: Integrator $e_{i\theta}$ in (38) is added on purpose to get a precise steady state. By doing so, we ensure that at steady state (when $\dot{\boldsymbol{e_z}} = 0$) we get the output at the right value. Note that this integrator will produce a pole at location zero. The location of this pole in closed loop (when $u = \boldsymbol{K}\boldsymbol{x}$, $\boldsymbol{K}$ computed by our proposed LQR method) will be in the left hand plane, i.e. the system becomes stable [25].

With the estimated curvature $\hat{\boldsymbol{z}}$ via extended Kalman filter (34), then the iterative LQR controller [25] is used to stabilize the linearized system at each time step, which guarantees the convergence speed and robustness of system by its advantage as the optimal controller, thus we replace $\boldsymbol{z}$ by $\hat{\boldsymbol{z}}$ in implementation. Concretely, by noting $\boldsymbol{e_z} = \boldsymbol{z_{eq}}(\theta_{L_{p_i}}) - \hat{\boldsymbol{z}}$ in the new state $\boldsymbol{x}$ of system, in order to minimize the following cost function:

$$\mathcal{J} = \int_{t_i}^{\infty} (\boldsymbol{x}^T\bar{\boldsymbol{Q}}\boldsymbol{x} + \bar{u}^T\bar{\boldsymbol{R}}\bar{u})dt,$$

where t_i is the initial time when end-effector enters the current linearized zone of $\theta_{L_{p_i}}$, $\bar{\boldsymbol{R}}$ and $\bar{\boldsymbol{Q}}$ are the weight matrices for $\bar{u}$ and $\boldsymbol{x}$, the following analytical solution of LQR controller is obtained:

$$\bar{u} = u_{LQR} = \bar{\boldsymbol{R}}^{-1}\bar{\boldsymbol{B}}\bar{\boldsymbol{P}}\boldsymbol{x}, \tag{39}$$

with $\bar{\boldsymbol{P}}$ is the solution of the following algebraic Riccati equation:

$$\bar{\boldsymbol{A}}\bar{\boldsymbol{P}} + \bar{\boldsymbol{P}}\bar{\boldsymbol{A}}^T + \bar{\boldsymbol{Q}} - \bar{\boldsymbol{P}}\bar{\boldsymbol{B}}^T\bar{\boldsymbol{R}}^{-1}\bar{\boldsymbol{B}}\bar{\boldsymbol{P}} = 0.$$

Thus, the input voltage $u = u_{LQR} + u_{eq}(\theta_{L_{p_i}})$.

V. Numerical simulation & Experiment

In this section, experimental tests will be presented to valid the deduced nonlinear model, and the proposed LQR controller.

A. Experimental setup

As shown in Fig. 4, our platform contains the polymer actuator which is connected to Arduino card and a camera (Microscope USB Dino-Lite) which enables us to catch the deformation of actuator with 20 fps. Specific image processing program has been developed by us to track the shape of polymer actuator in real time and compute the corresponding curvatures and its time derivatives for each divided segment, which will be detailed in the next subsection. Tab.I shows the measured parameters of the tested actuator.

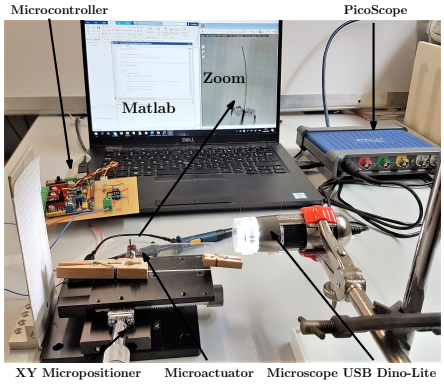

Fig. 4. Experiment device. The actuator is fixed on the workbench and charged by micro-controller (MakeBlock MegaPi). A Dino-Lite micro camera on the right side is installed for observing the deformation of actuator.

B. Nonlinear model validation

1) Parameter identification: In order to identify the unknown parameters (q_1, q_2, q_3), we use a ramp signal $V_{in} = at$ with $a = 0.01\ V/s$ as the excitation input signal to deform the polymer. In the work of Section III, the variable $\boldsymbol{z}$ is calculated

TABLE I
MEASURED PARAMETERS

Length L	Width b	Thickness h
5.87 mm	1.37 mm	0.035 mm
Strain to stress ratio α	Mean Young's modulus E	Mass density ρ
7.31×10^{-10}m^3/C	2.53 GPa	2.42×10^3 kg/m^3

from the curvature of actuator, which can be measured directly by our designed visual system. Since the actuation speed is very low, the actuator can be regarded as quasi-static state. Since there is no external force applied on the actuator, the internal force equals to the actuation one, i.e., for $s \in [0,\ L]$, $\boldsymbol{\Lambda}_i(s) = \boldsymbol{\Lambda}_a(s)$, which means:

$$\kappa(s,t) = \frac{\beta\lambda(s,t)}{\mathrm{EI_z}} = \frac{z(s,t)}{\mathrm{EI_z}}, \tag{40}$$

where κ is the curvature along axis z of polymer actuator. Thus z can be calculated by observing κ:

$$z(s,t) = \mathrm{EI_z}\kappa(s,t). \tag{41}$$

Based on the image captured by the rapid camera, the shape of actuator can be extracted, from which we can compute the curvature along actuator and its derivative of time. An algorithm of image binarization, inter-frame difference [26] and skeleton extraction [27] is applied via Matlab for obtaining the center skeleton of actuator. Then the curvature could be calculated by the following equation:

$$\kappa = \frac{y''}{(1+y'^2)^{3/2}},\ \dot{\kappa} = \frac{\partial\kappa}{\partial t}. \tag{42}$$

However, it is inconvenient to compute the curvature and its derivative directly by the point data set of skeleton, due to the repeated calculation and discontinuity of data. To overcome this problem a polynomial curve fitting method is used here to get the curve function of actuator in real time which is of the following form:

$$y = \sum_{i=0}^{w} p_i x^i. \tag{43}$$

The analytical expression of the curvature and its derivative can be obtained directly by taking (43) into (42):

$$\kappa = \frac{\sum_{i=0}^{w} i(i-1)p_i x^{i-2}}{(1+(\sum_{i=0}^{w} ip_i x^{i-1})^2)^{3/2}},\ \dot{\kappa} = \frac{\partial\kappa}{\partial t}. \tag{44}$$

Based on the methods above, we got the curvature and its derivative of all sections as shown in Fig. 5. From the figure we can observe that the overall derivative of curvature of the actuator shows a trend of increasing first and then becoming steady. This is because the charge inside actuator gradually reaches saturation from the near power end (section 1) to the far power end (section 10). From the physical analysis

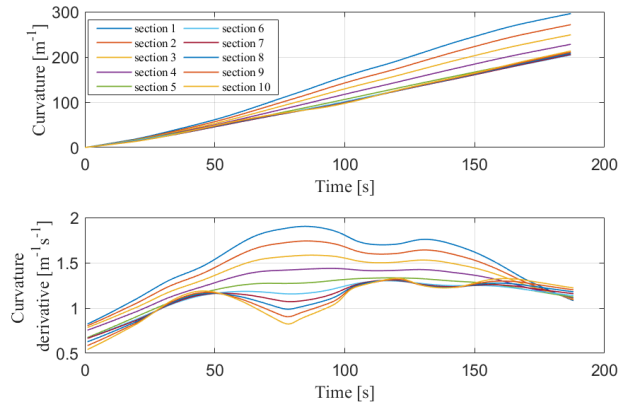

Fig. 5. Curvature and its derivative measured under input $u = 0.01t$.

about the micro structure of conducting polymer actuator [15], the resistance of the inter-layer is little varied by the charge density. Thus it is reasonable to suppose that q_2 in our model is constant, which mostly corresponds to the ionic mass transport. On the contrary, there exists a variation of conductivity and volumetric capacitance of the electrode which can not be ignored during the procedure of charge [15]. Indeed the electrical conductivity of the conducting polymer is a nonlinear function of redox level and the volumetric capacitance changes with the oxidation state. Hence, in the identification process, we finally adopt the following 5-order polynomial to represent the nonlinearity of q_1, and q_3:

$$q_1(s) = \sum_{i=0}^{5} a_i s^i\ ,\ q_2(s) = b_0\ ,\ q_3(s) = \sum_{i=0}^{5} c_i s^i.$$

The identified values are given in Tab. II.

2) Comparison and validation: In order to show the deduced model is reliable, we simulate our model with the identified nonlinearity of q_1, q_2 and q_3, and compare the deformation result with experimental measurements. Fig. 6 shows the evolution of the curvature for the 1st section, the 5th section and the 10th section, indicating the fitting level between the experiment and the deduced model with the parameter fitting function of 4 order and 5 order. The error

TABLE II
IDENTIFIED RESULT OF q_1, q_2, q_3

i	0	1	2	3	4	5
a_i	526	249	-6.814	0.111	$-6.9e^{-4}$	$1.4e^{-6}$
b	0.0275					
c_i	0.0110	$-5.9e^{-5}$	$-2.4e^{-7}$	$6.1e^{-9}$	$2.8e^{-11}$	$4.2e^{-14}$

percentage of average curvature of the latter is less than 5% which is acceptable in our study. Fig. 7 shows the coincidence

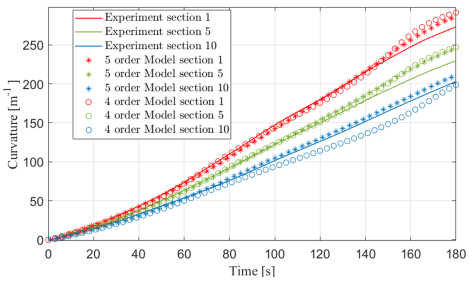

Fig. 6. The evolution of the curvature for each segment of the actuator.

level of the deformation of actuator with time between the experiment and the simulation via quasi-static model and dynamic model, under a ramp input voltage $u = 0.0075t$ and a step input voltage of amplitude 1.5V respectively. An

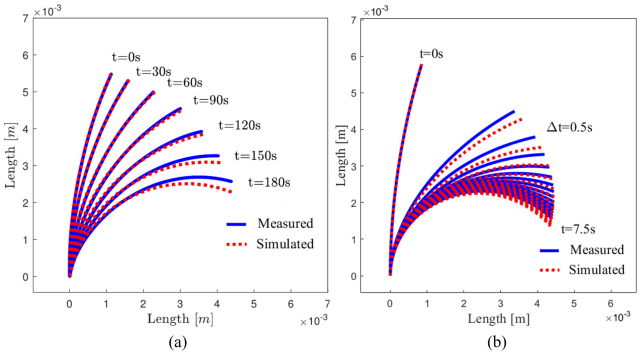

Fig. 7. (a). Deformation of the polymer actuator under the ramp input comparing with mechanical static model; (b). Deformation of the polymer actuator under the step input comparing with mechanical dynamic model.

experiment with external load is also carried out. As shown in Fig.8, a payload mass of 63mg is fixed on the tip of actuator. In this case, by changing the boundary condition of (15) to:

$$\mathbf{\Lambda}_{\mathrm{i}}(\mathrm{L}) - \mathbf{\Lambda}_{\mathrm{a}}(\mathrm{L}) + \mathrm{Ad}_{\boldsymbol{g}_{\mathrm{L}}}^{-1}\mathcal{M}_{\mathrm{p}}\mathcal{G} = \mathcal{M}_{\mathrm{p}}\dot{\boldsymbol{\eta}}_{\mathrm{L}} - \mathrm{ad}_{\boldsymbol{\eta}_{\mathrm{L}}}^{\mathrm{T}}\mathcal{M}_{\mathrm{p}}\boldsymbol{\eta}_{\boldsymbol{L}},$$

one can deduce the mechanical dynamics model of actuator in case of adding payload, where $\mathcal{M}_p$ is the inertial matrix of payload and $\mathrm{Ad}_{\boldsymbol{g}_{\mathrm{L}}}$ is the transformation matrix (see appendix). The comparison between simulation and experiment is shown in Fig.8 under the step input voltage of amplitude 1.5V and 0.1Hz.

C. Orientation control

Two control tests were implemented respectively for moving to fixed orientation and tracking a variable reference.

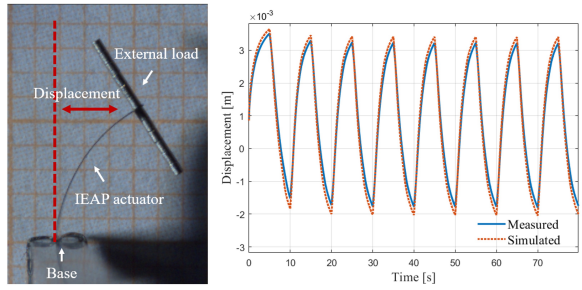

Fig. 8. Displacement of tip of the polymer actuator with external load under the step input voltage of amplitude 1.5V and 0.1Hz comparing with mechanic dynamic model.

1) Moving to fixed orientation: It is expected to control polymer's end-effector orientation θ_L to a given desired orientation $\theta_{L_{fin}}$ from its initial orientation $\theta_{L_{ini}}$. A linear trajectory is planned to avoid input saturation (i.e., $V_{in} \leq 3V$) and ensures that the actuator might arrive at desired orientation in a stable speed. Therefore, we have the following output reference with $k = 2.5$:

$$\theta_{L_{ref}} = \begin{cases} kt + \theta_{L_{ini}}, & t < \frac{\theta_{L_{fin}} - \theta_{L_{ini}}}{k} \\ \theta_{L_{fin}}, & t \geqslant \frac{\theta_{L_{fin}} - \theta_{L_{ini}}}{k} \end{cases}$$

where $\theta_{L_{ini}} = \pi/12$, $\theta_{L_{fin}} = \pi/4$ and $k = 0.045$.

2) Tracking variable reference: A sinusoidal reference is tested in the experiment, which is as follows:

$$\theta_{L_{ref}} = \theta_{L_{ini}} + \theta_a sin(\omega t),$$

where the initial orientation $\theta_{L_{ini}} = \pi/6$, amplitude $\theta_a = \pi/25$ and frequency $\omega = 0.02$ rad/s.

3) Parameter setting: By following the proposed procedure in Section V, we first linearize the deduced nonlinear model in each zone, and then an Extended Kalman filter of form (34) has been constructed with $\boldsymbol{Q} = 10\mathbf{I}$ and $\boldsymbol{R} = 0.01$. After that, the proposed LQR controller of form (39) has been realized with $\bar{\boldsymbol{Q}} = diag\{1, ..., 1, 10\} \in \mathbb{R}^{11\times 11}$ and $\bar{\boldsymbol{R}} = 100$.

4) Result analysis: The corresponding experimental results have been depicted in Fig. 9 and Fig. 10. Clearly, we can observe that the trajectory of polymer's end-effector can track the reference trajectory accurately with an error within 1%. The system can maintain stable when an external vibration disturbance was applied on it. Additionally, the input signal is within $3V$, which is in the ideal input region.

VI. CONCLUSION

In this paper, a nonlinear modeling and control for conducting polymer actuator are investigated. The study focuses on electric and mechanic model, allowing to consider nonlinearity which occurs in the micro-actuator. Electro-mechanical model is proposed, based on which the parameter identification approach has been addressed where measured curvatures are well predicted by the deduced model. Then controller design using Linear–Quadratic Regulator is proposed, where an Extended Kalman filter has been introduced to estimate polymer's curvatures. With the proposed LQR controller, actuator bending angle is then controlled where measurements are in good

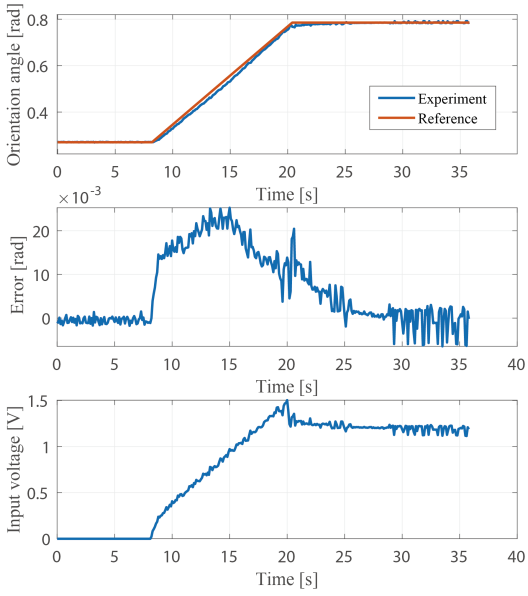

Fig. 9. Control performance of tracking ramp reference.

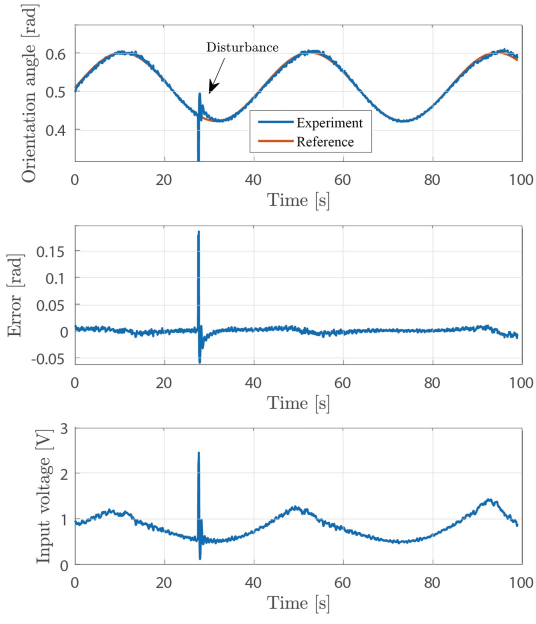

Fig. 10. Control performance of tracking sinusoidal reference.

agreement with the imposed bending angle. The results of this study is illustrated with simulation and experimental validations. Future work would focus on the design and control for multi-body (in series/parallel) micro-robot based on IEAP actuators, in order to validate the final application (such as robots for navigation in vessel and micro gripper).

Acknowledgment

This work was supported by the French Government through the National Research Agency (ANR) : ROBOCOP (ANR-19-CE19), PIA EQUIPEX LEAF (ANR-11-EQPX-0025) projects, H2020 project TWINNIMS (Grant agreement 857263), and the French RENATECH network.

Appendix

A. Lie group notations

The adjoint representation of the Lie algebra is given by

$$\mathrm{ad}_{\boldsymbol{\xi}} = \begin{pmatrix} \tilde{\boldsymbol{\kappa}} & \mathbf{0}_{3\times3} \\ \tilde{\boldsymbol{\epsilon}} & \tilde{\boldsymbol{\kappa}} \end{pmatrix} \in \mathbb{R}^{6\times6}, \ \mathrm{ad}_{\boldsymbol{\eta}} = \begin{pmatrix} \tilde{\boldsymbol{w}} & \mathbf{0}_{3\times3} \\ \tilde{\boldsymbol{v}} & \tilde{\boldsymbol{w}} \end{pmatrix} \in \mathbb{R}^{6\times6},$$

where the operator $\tilde{(\cdot)}$ represents a conversion from a 3-dimensional vector to its skew-symmetric matrix.

B. Transformation matrix

The matrix transforming the velocity or acceleration twist from body frame to inertial frame is given by

$$\mathrm{Ad}_{\boldsymbol{g}(X)} = \begin{pmatrix} \boldsymbol{R} & \mathbf{0}_{3\times3} \\ \tilde{\boldsymbol{u}}\boldsymbol{R} & \boldsymbol{R} \end{pmatrix} \in \mathbb{R}^{6\times6}.$$

References

[1] G. Kaur, R. Adhikari, P. Cass, M. Bown, and P. Gunatillake, "Electrically conductive polymers and composites for biomedical applications," *Rsc Advances*, vol. 5, no. 47, pp. 37 553–37 567, 2015.

[2] H. He, L. Zhang, X. Guan, H. Cheng, X. Liu, S. Yu, J. Wei, and J. Ouyang, "Biocompatible conductive polymers with high conductivity and high stretchability," *ACS applied materials & interfaces*, vol. 11, no. 29, pp. 26 185–26 193, 2019.

[3] E. Smela, "Conjugated polymer actuators for biomedical applications," *Advanced materials*, vol. 15, no. 6, pp. 481–494, 2003.

[4] T. F. Otero, "Towards artificial proprioception from artificial muscles constituted by self-sensing multi-step electrochemical macromolecular motors," *Electrochimica Acta*, vol. 368, p. 137576, 2021.

[5] F. Vidal, C. Plesse, D. Teyssié, and C. Chevrot, "Long-life air working conducting semi-ipn/ionic liquid based actuator," *Synthetic Metals*, vol. 142, no. 1-3, pp. 287–291, 2004.

[6] M. Ghaffari, W. Kinsman, Y. Zhou, S. Murali, Q. Burlingame, M. Lin, R. Ruoff, and Q. Zhang, "Retracted: Aligned nano-porous microwave exfoliated graphite oxide ionic actuators with high strain and elastic energy density," *Advanced Materials*, vol. 25, no. 43, pp. 6277–6283, 2013.

[7] L. Seurre, K. Rohtlaid, G. T. Nguyen, C. Soyer, S. Ghenna, S. Grondel, F. Vidal, B. Cagneau, C. Plesse, and E. Cattan, "Demonstrating full integration process for electroactive polymer microtransducers to realize soft microchips," in *2020 IEEE 33rd International Conference on Micro Electro Mechanical Systems (MEMS)*. IEEE, 2020, pp. 917–920.

[8] I. Must, V. Vunder, F. Kaasik, I. Põldsalu, U. Johanson, A. Punning, and A. Aabloo, "Ionic liquid-based actuators working in air: The effect of ambient humidity," *Sensors and Actuators B: Chemical*, vol. 202, pp. 114–122, 2014.

[9] K. J. Kim and S. Tadokoro, "Electroactive polymers for robotic applications," *Artificial Muscles and Sensors*, vol. 23, p. 291, 2007.

[10] C. Plesse, F. Vidal, H. Randriamahazaka, D. Teyssié, and C. Chevrot, "Synthesis and characterization of conducting interpenetrating polymer networks for new actuators," *Polymer*, vol. 46, no. 18, pp. 7771–7778, 2005.

[11] C. H. Nguyen, G. Alici, and G. Wallace, "An advanced mathematical model and its experimental verification for trilayer conjugated polymer actuators," *IEEE/ASME Transactions on Mechatronics*, vol. 19, no. 4, pp. 1279–1288, 2013.

[12] A. Mazzoldi, A. Della Santa, and D. De Rossi, "Conducting polymer actuators: Properties and modeling," in *Polymer sensors and actuators*. Springer, 2000, pp. 207–244.

[13] K. Rohtlaid, L. Seurre, G. T. Nguyen, G. Curley, C. Soyer, S. Grondel, F. Vidal, C. Plesse, and E. Cattan, "Pedot: Pss-based micromuscles and microsensors fully integrated in flexible chips," *Smart Materials and Structures*, vol. 29, no. 9, p. 09LT01, 2020.

[14] M. Farajollahi, F. Sassani, N. Naserifar, A. Fannir, C. Plesse, G. T. Nguyen, F. Vidal, and J. D. Madden, "Characterization and dynamic charge dependent modeling of conducting polymer trilayer bending," *Smart Materials and Structures*, vol. 25, no. 11, p. 115044, 2016.

[15] M. Farajollahi, A. Usgaocar, Y. Dobashi, V. Woehling, C. Plesse, F. Vidal, F. Sassani, and J. D. Madden, "Nonlinear two-dimensional transmission line models for electrochemically driven conducting polymer actuators," *IEEE/ASME Transactions on Mechatronics*, vol. 22, no. 2, pp. 705–716, 2016.
[16] G. Nishida, K. Takagi, B. Maschke, and T. Osada, "Multi-scale distributed parameter modeling of ionic polymer-metal composite soft actuator," *Control Engineering Practice*, vol. 19, no. 4, pp. 321–334, 2011.
[17] A. A. A. Moghadam, A. Kouzani, K. Torabi, A. Kaynak, and M. Shahinpoor, "Development of a novel soft parallel robot equipped with polymeric artificial muscles," *Smart Materials and Structures*, vol. 24, no. 3, p. 035017, 2015.
[18] N. Liu, Y. Wu, and Y. Le Gorrec, "Energy-based modeling of ionic polymer–metal composite actuators dedicated to the control of flexible structures," *IEEE/ASME Transactions on Mechatronics*, vol. 26, no. 6, pp. 3139–3150, 2021.
[19] J. Khawwaf, J. Zheng, R. Chai, R. Lu, and Z. Man, "Adaptive microtracking control for an underwater ipmc actuator using new hyperplane-based sliding mode," *IEEE/ASME Transactions on Mechatronics*, vol. 24, no. 5, pp. 2108–2117, 2019.
[20] N. T. Nguyen, Y. Dobashi, C. Soyer, C. Plesse, G. T. Nguyen, F. Vidal, E. Cattan, S. Grondel, and J. D. Madden, "Nonlinear dynamic modeling of ultrathin conducting polymer actuators including inertial effects," *Smart Materials and Structures*, vol. 27, no. 11, p. 115032, 2018.
[21] C. B. Black, J. Till, and D. C. Rucker, "Parallel continuum robots: Modeling, analysis, and actuation-based force sensing," *IEEE Transactions on Robotics*, vol. 34, no. 1, pp. 29–47, 2017.
[22] F. Boyer, V. Lebastard, F. Candelier, and F. Renda, "Dynamics of continuum and soft robots: A strain parameterization based approach," *IEEE Transactions on Robotics*, vol. 37, no. 3, pp. 847–863, 2020.
[23] F. Renda, F. Boyer, J. Dias, and L. Seneviratne, "Discrete cosserat approach for multisection soft manipulator dynamics," *IEEE Transactions on Robotics*, vol. 34, no. 6, pp. 1518–1533, 2018.
[24] M. I. Ribeiro, "Kalman and extended kalman filters: Concept, derivation and properties," *Institute for Systems and Robotics*, vol. 43, p. 46, 2004.
[25] J. P. Hespanha, *Linear systems theory*. Princeton university press, 2018.
[26] Y. H. Cheng and J. Wang, "A motion image detection method based on the inter-frame difference method," in *Applied Mechanics and Materials*, vol. 490. Trans Tech Publ, 2014, pp. 1283–1286.
[27] F. Zhao and X. Tang, "Preprocessing and postprocessing for skeleton-based fingerprint minutiae extraction," *Pattern Recognition*, vol. 40, no. 4, pp. 1270–1281, 2007.

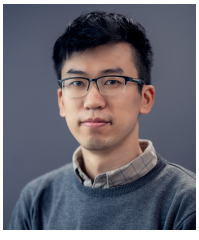

Lingxiao Xun received the B.E degree in mechanical engineering from Nanjing University of Aeronautics and Astronautics, Nanjing, China, in 2017 and a M.E degree in Mechatronics system from ENSAM, France, in 2019. He is now a Ph.D. candidate in robotics at INRIA, Lille, France. His research interests include mechatronics, automation and robotics.

Gang Zheng received the B.E. and M.E. degrees in Communication and systems from Wuhan University, China, in 2001 and 2004, respectively, and the Ph.D. degree in automatic control from ENSEA, Cergy-Pontoise, France, in 2006. Since 2007, he has held postdoctoral positions at INRIA Grenoble, at the Laboratoire Jean Kuntzmann, and at ENSEA. He joined INRIA Lille as a permanent researcher from September 2009.

Sofiane Ghenna received a master's degree in electrical engineering systems from the National Polytechnic Institute - ENSEEIHT Toulouse in 2012. He received a Ph.D. degree in electrical engineering from Lille University, France in 2016. He is currently an Associate Professor at Université Polytechnique Hauts-de-France Valenciennes, France. His research interests include modeling and control of smart material-based actuators.

Alexandre Kruszewski (39 y/o, male, Full Professor, first-time participant to FET H2020) is a full professor at Centrale Lille Institutes. He is a member of the joint team (CRIStAL UMR 9189 – Inria) Defrost. He has a strong experience (both theoretical and practical) in the robust control design based on numerical optimization. Since 2015, his main research topic is the control design of soft robots based on Finite Element Methods.

Éric Cattan received his Ph.D. from the university Paris XI Orsay in 1993. He was then recruited as an Associate Professor in the Laboratory of Advanced Ceramic Materials in 1994. He then joined the Institute of Electronics and Microelectronics and Nanotechnologies at the University of Polytechnic Hauts de France, and he became a Professor in 2002. His career began in the field of piezoelectric and ferroelectric thin films, and the last twenty years have been devoted to bioinspired MEMS.

Christian Duriez received the engineering degree from the Institut Catholique d'Arts et Métiers of Lille, France and a PhD degree in robotics from University of Evry, France. His thesis work was realized at CEA/ Robotics and Interactive Systems Technologies followed by a postdoctoral position at the CIMIT SimGroup in Boston. He arrived at INRIA in 2006 to work on interactive simulation of deformable objects, haptic rendering and medical simulation. He is now the head of DEFROST team, created in January 2015.

Sébastien Grondel received M.S. and Ph.D. degrees in electronic and mechanical engineering from Université Polytechnique Hauts-de-France, France, in 1997 and 2000, respectively. Between 2001 and 2010, he worked as a Research Associate at the Electronic, Microelectronic and Nanoelectronic Department at the Université Polytechnique Hauts-de-France, focusing on structural health monitoring and medical acoustic imaging. Since 2011, he has been a Professor in the same department and teacher at the engineering school INSA Hauts-de-France.